


Cite this: *J. Mater. Chem. A*, 2022, **10**, 7754

Design of 3D topological nodal-net porous carbon for sodium-ion battery anodes

Dongyuan Ni, Yiheng Shen, Wei Sun and Qian Wang *

Based on first-principles calculations, we propose a new 3D topological nodal-net carbon allotrope consisting of graphene nanoribbons. This structure possesses orthorhombic symmetry with 46 carbon atoms in its primitive cell, termed oC46, which is energetically, thermally, and dynamically stable. More interestingly, a Dirac nodal net composed of three types of nodal lines is found in its first Brillouin zone, where the nodal lines are protected by the coexistence of time-reversal, spatial inversion, and mirror/glide-plane symmetries. These features can be characterized by effective $k \cdot p$ models. In addition, oC46 is found to be a promising anode material for sodium-ion batteries with a high reversible capacity of 303 mA h g^{-1} , a low diffusion energy barrier (0.05 eV) for Na ions, an appropriate average voltage of 0.43 V, and a small volume change of 2.0% during charging/discharging operation. The main reasons for the high performance are uncovered to be due to the ordered porosity of the structure and the Dirac massless fermions induced by the nodal net, which provide a large number of sodium-ion adsorption sites and enhance the electric conductivity of both electrons and ions. These findings make this system promising for Na-ion batteries.

Received 24th January 2022
Accepted 23rd February 2022

DOI: 10.1039/d2ta00652a

rsc.li/materials-a

1. Introduction

Sodium-ion batteries (SIBs) have attracted increasing attention in recent years due to the high abundance in the continental crust and environmentally friendly nature of sodium. However, the anodes for lithium-ion batteries (LIBs) usually exhibit poor performance when used for SIBs, showing low energy density, large volume expansion, and low coulombic efficiencies.¹ For example, graphite, as the successfully commercialized LIB anode material, exhibits a fairly low capacity of 35 mA h g^{-1} when acting as an anode for SIBs.² The main reason is due to the larger atomic radius of sodium atoms as compared to lithium. Therefore, considerable effort has been devoted to the design and synthesis of new anode materials for SIBs. For instance, it was found that titanium oxides and titanium phosphates have impressive rate capability and long cycle life, while their electric conductivity is quite low.³ Alloy-based anodes can achieve high capacity and low volume expansion, but usually have fairly high diffusion barriers for sodium ions.⁴ In addition, conversion-based anode materials, which adsorb sodium ions through conversion reaction, exhibit considerable voltage hysteresis and large volume changes.^{4,5} Compared to these anode materials, carbon materials have advantages because the flexible bonding and orbital hybridization of carbon atoms not only can result in various allotropes with porous geometric structures for the storage and transport of sodium ions, but also offer delocalized

electrons for introducing metallicity or semimetallicity that can improve their electronic conductivity. Thus, it is highly desirable to explore high-performance carbon anode materials for SIBs.

Topological semimetallic porous carbon materials are of particular interest, due to their intrinsic high conductivity protected by their topology. For the electronic properties, the crossing feature of the conduction and valence bands near the Fermi level can excite Dirac fermions, and then improve the electronic conductivity of such systems.⁶ So far, the reported topological carbon semimetals include Dirac semimetals,^{7,8} Weyl semimetals,^{9–13} nodal-line semimetals,^{14–16} nodal-link semimetals,¹⁷ nodal-knot semimetals,¹⁸ nodal-chain semimetals,^{19,20} nodal-net semimetals,²¹ and nodal-surface semimetals,^{22,23} while a nodal line semimetal is found to carry a non-trivial Berry phase π along the loop which encircles the nodal line. The symmetry-based topological protection mechanisms of nodal lines are either *via* the coexistence of time-reversal symmetry T and spatial inversion symmetry P , or by mirror/glide-plane symmetry.²⁴ In experiments, it has been found that some extremely high-mobility charge carriers exist in nodal-line semimetals due to the Dirac-like dispersion, and the density of the nodal-line fermions is much higher than that of the Dirac fermions in topological semimetals with discrete nodes.¹⁶ Therefore, nodal-net semimetals with multiple nodal lines should more easily excite high-mobility carriers. This stimulates studies on topological semimetallic carbon materials for SIB anodes. It has been found that nodal-line²⁵ and nodal-surface²⁶ semimetals are promising anode materials for

School of Materials Science and Engineering, CAPT, BKL-MEMD, Peking University, Beijing, China. E-mail: qianwang2@pku.edu.cn

SIBs. However, no study has been reported on designing nodal-net semimetals for battery applications despite the fact that more nodal-line fermions can be excited for further enhancing the carrier mobility in such materials.

In this work, we design a new stable 3D porous carbon allotrope, named oC46, and show its interesting electronic features, *i.e.*, there are three types of nodal lines protected by the coexistence of spatial inversion, time-reversal, and mirror/glide-plane symmetries, exhibiting drumhead surface states formed by connecting nodal lines of the same type. We further demonstrate that oC46 can be used as an anode material for SIBs with good performance.

2. Computational methods

First-principles calculations within the framework of density functional theory are performed by using the Vienna *ab initio* simulation package (VASP).²⁷ The projector augmented wave (PAW) method²⁸ is employed to treat the interactions between the ion cores and valence electrons. A plane-wave basis set with an energy cutoff of 600 eV is used to expand the valence electron wavefunctions. The exchange–correlation potential between electrons is treated by using the Perdew–Burke–Ernzerhof functional (PBE)²⁹ within the generalized gradient approximation (GGA).³⁰ The Heyd–Scuseria–Ernzerhof hybrid functional (HSE06)³¹ is further used for high-accuracy electronic structure calculations. The first Brillouin zone is represented by a $3 \times 3 \times 7$ k -points mesh within the Monkhorst–Pack scheme.³² The

convergence thresholds for the total energy and force are set to 10^{-4} eV and 10^{-2} eV \AA^{-1} , respectively, for geometry optimization, which are respectively raised to 10^{-8} eV and 10^{-6} eV \AA^{-1} for phonon calculations that are carried out by using the finite displacement method³³ implemented in the PHONOPY package.³⁴ The elastic constants are calculated by using the energy-strain method implemented in the AELAS package.³⁵ *Ab initio* molecular dynamics (AIMD) simulations are carried out to verify the thermal stability of the designed system with the canonical ensemble, where the temperature is controlled by using the Nosé thermostat.³⁶ The topological properties and surface states are studied by using the WANNIERTOOLS package³⁷ based on the maximally localized Wannier functions.³⁸ The climbing-image nudged elastic band (CI-NEB) method³⁹ is used to calculate the diffusion barriers of Na ions.

3. Results and discussion

3.1. Geometry, stability, and mechanical properties

We construct a 3D porous carbon allotrope by using zigzag graphene nanoribbons with the width of a double-benzene-ring and connecting seven such nanoribbons with the sp^3 -hybridized carbon chains as linkers (see Fig. 1(a)), forming a primitive cell, as shown in Fig. 1(b). After full optimization, the structure possesses an orthorhombic symmetry in the nonsymmorphic space group $Cmcm$ (no. 63) and contains 46 atoms per primitive cell, as shown in Fig. 1(c) (dashed frame), thus termed oC46. In addition, Fig. 4(d) shows a perspective view of a $2 \times 2 \times 7$

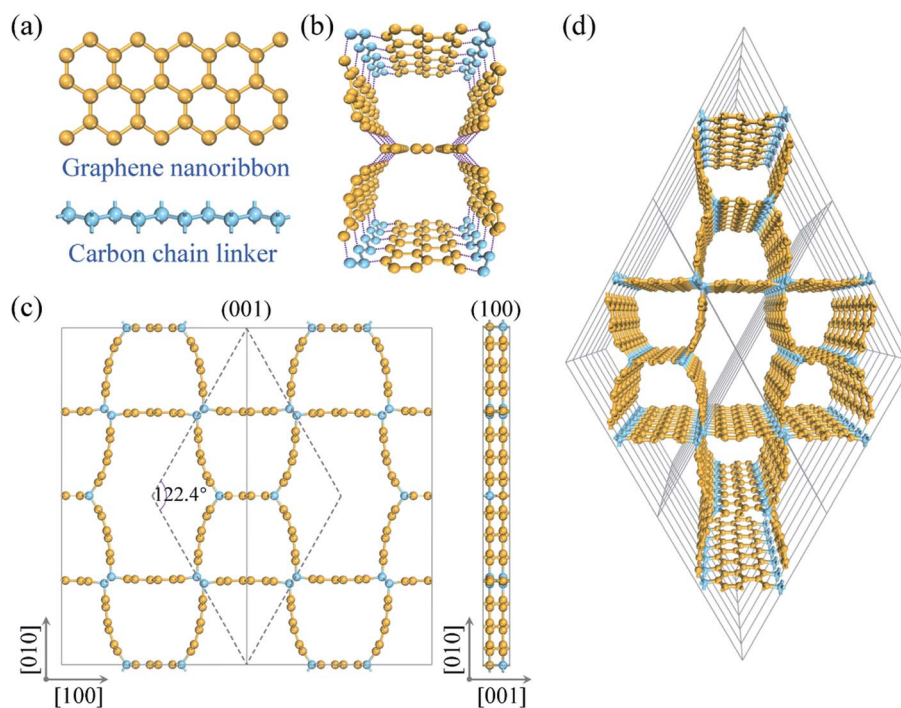


Fig. 1 (a) Building block of the zigzag graphene nanoribbon and sp^3 -hybridized carbon chain linker. (b) Assembling process of the building blocks and the linkers. (c) Optimized geometry of oC46. The dashed frame and solid rectangles represent the primitive and unit cells, respectively. (d) Perspective view of a $2 \times 2 \times 7$ supercell of the oC46's primitive cell. The orange and blue spheres represent the three-fold coordinated and four-fold coordinated carbon atoms, respectively.

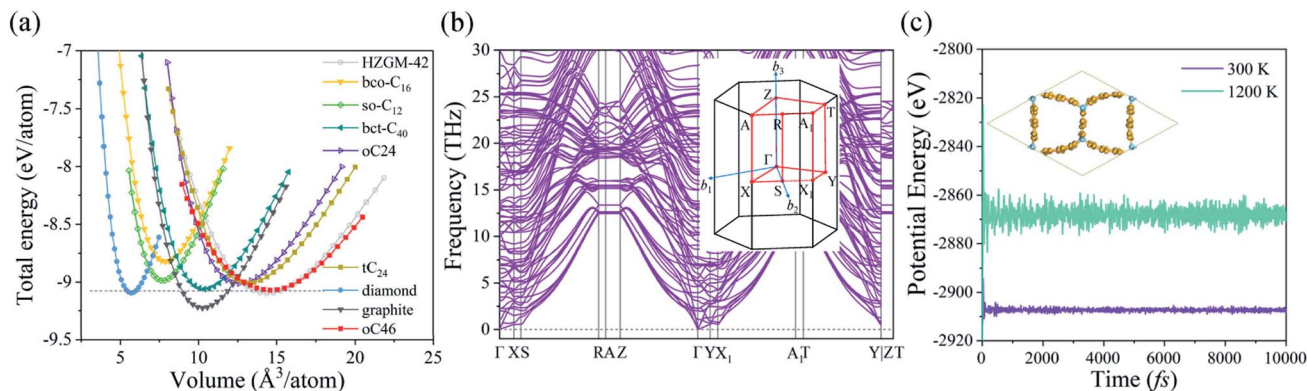


Fig. 2 (a) Calculated energy–volume curve of oC46, compared with diamond, graphite, and previous reported semimetallic carbon allotropes. (b) Phonon spectrum of oC46 along the high symmetry q -point path in its first Brillouin zone. (c) Total potential energy fluctuation during AIMD simulation at 300 and 1200 K, respectively. The inset in (c) shows the atomic configuration of oC46 ($1 \times 1 \times 7$ supercell of its primitive cell) at the end of the simulation at 1200 K.

supercell of the oC46's primitive cell, exhibiting the regularly porous structure of oC46.

To study the energetic stability of oC46, the change of the average binding energy per atom with the volume is calculated. We firstly do geometry relaxation for the primitive cell to obtain the optimized structure with convergence thresholds of 10^{-8} eV and 10^{-6} eV \AA^{-1} for the total energy and force, respectively. Then, we change the volume of the optimized structure by setting different universal scaling factors for the lattice constants from 0.85 to 1.15 by an increment of 0.01. For each volume-changed structure, we do optimization to get the total energy with fixed lattice constants, based on which the energy and volume per atom are obtained. For comparison, calculations are also carried out for some 3D semimetallic carbon allotropes, including HZGM-42,⁴⁰ bco-C₁₆,⁴¹ so-C₁₂,⁴² bct-C₄₀,⁴³ oC24,⁴⁴ tC₂₄,²⁶ and for diamond and graphite. The results are plotted in Fig. 2(a). One can see that except for graphite, diamond, and HZGM-42, oC46 possesses the lowest energy. The calculated bond lengths between the three-fold coordinated carbon atoms are in the range of 1.35–1.46 \AA , which are comparable to that of the sp^2 -hybridized carbon atoms of graphite (1.42 \AA), and the corresponding bond angles are in the range of 117.1–121.4°, close to that of graphite (120°). The bond length between the four-fold coordinated carbon atoms is 1.53 \AA , the same as the sp^3 -hybridized carbon atoms in diamond, and the bond angle is 108.1°, close to that of diamond (109.5°). Thus, the reason for the high energetic stability of oC46 could be the suitable values of bond lengths and bond angles. To verify the dynamical stability of oC46, the phonon spectrum is calculated by using the finite displacement method.³³ As shown in Fig. 2(b), no imaginary frequency mode appears in the entire Brillouin zone, confirming that oC46 is dynamically stable. The thermal stability of oC46 is examined by performing the AIMD simulation from 300 K to 1200 K for 10 ps with a timestep of 1 fs, as shown in Fig. 2(c). A large $1 \times 1 \times 7$ supercell of the oC46's primitive cell is used to reduce the constraint associated with the periodic boundary condition. We find that the total potential energies fluctuate slightly around an average value during the entire simulation,

and the skeleton of oC46 remains almost intact at the end of simulation within the heating bath at 1200 K, confirming that oC46 is thermally stable even at the high temperature of 1200 K. Finally, the mechanical stability of oC46 is verified by Born–Huang criteria for an orthorhombic lattice: $C_{11} > 0$, $C_{22} > 0$, $C_{33} > 0$, $C_{44} > 0$, $C_{55} > 0$, $C_{66} > 0$, $[C_{11} + C_{22} + C_{33} + 2(C_{12} + C_{13} + C_{23})] > 0$, $(C_{11} + C_{22} - 2C_{12}) > 0$, $(C_{11} + C_{33} - 2C_{13}) > 0$, and $(C_{22} + C_{33} - 2C_{23}) > 0$.⁴⁵ The independent elastic constants of oC46 are calculated by using the energy-strain method implemented in the AELAS package,³⁵ which are $C_{11} = 198.1$ GPa, $C_{12} = 21.8$ GPa, $C_{13} = 29.0$ GPa, $C_{22} = 128.6$ GPa, $C_{23} = 26.6$ GPa, $C_{33} = 618.6$ GPa, $C_{44} = 137.4$ GPa, $C_{55} = 116.5$ GPa, and $C_{66} = 5.1$ GPa. The elastic constants fully satisfy the criteria listed above, confirming that oC46 is mechanically stable.

Next, to obtain the maximum tensile strength, we use the quasi-static displacement-controlled deformation in three orthogonal directions with a strain increment of 0.01. The results are shown in Fig. 3. For oC46, the maximum stress along the [100]-, [010]-, and [001]-directions is 16.9, 26.3, and 69.2 GPa, corresponding to the maximum tensile strain of 14%, 15%, and 20%, respectively. As a comparison, the mechanical properties of an interpenetrating-silicene-network SIB anode material, named ISN, with a nodal-line characteristic of its electronic band structure,²⁵ are also calculated and plotted in Fig. 3, which shows that the maximum stress of oC46 is higher than that of ISN in all three directions, indicating that the mechanical properties of oC46 are good enough for the application of SIB anodes.

3.2. Electronic properties

We next discuss the electronic properties of oC46. In the absence of spin–orbit coupling (SOC), oC46 is a semimetal as deduced by its electronic band structure calculated at the GGA-PBE level, as shown in Fig. 4(a). Note that the valence and conduction bands exhibit linear dispersion near the Fermi level along the Z - Γ , X_1 - A_1 , and T - Y paths. To validate the semimetallic feature, we recalculate the band structure at the HSE06 (ref. 31) level. The results are also plotted in Fig. 4(a), which

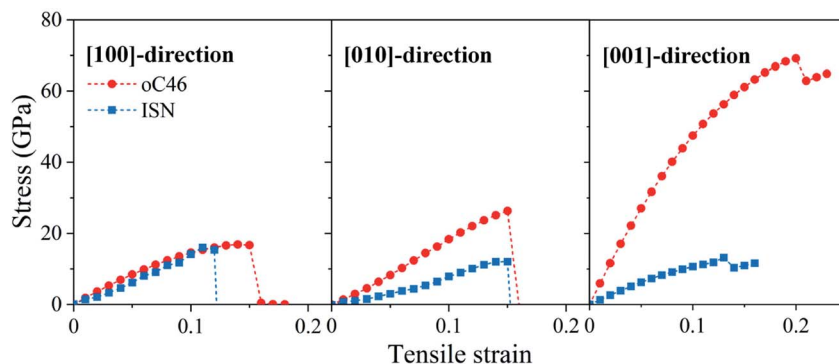


Fig. 3 Variation of the stress with axial tensile strain in oC46 and ISN.

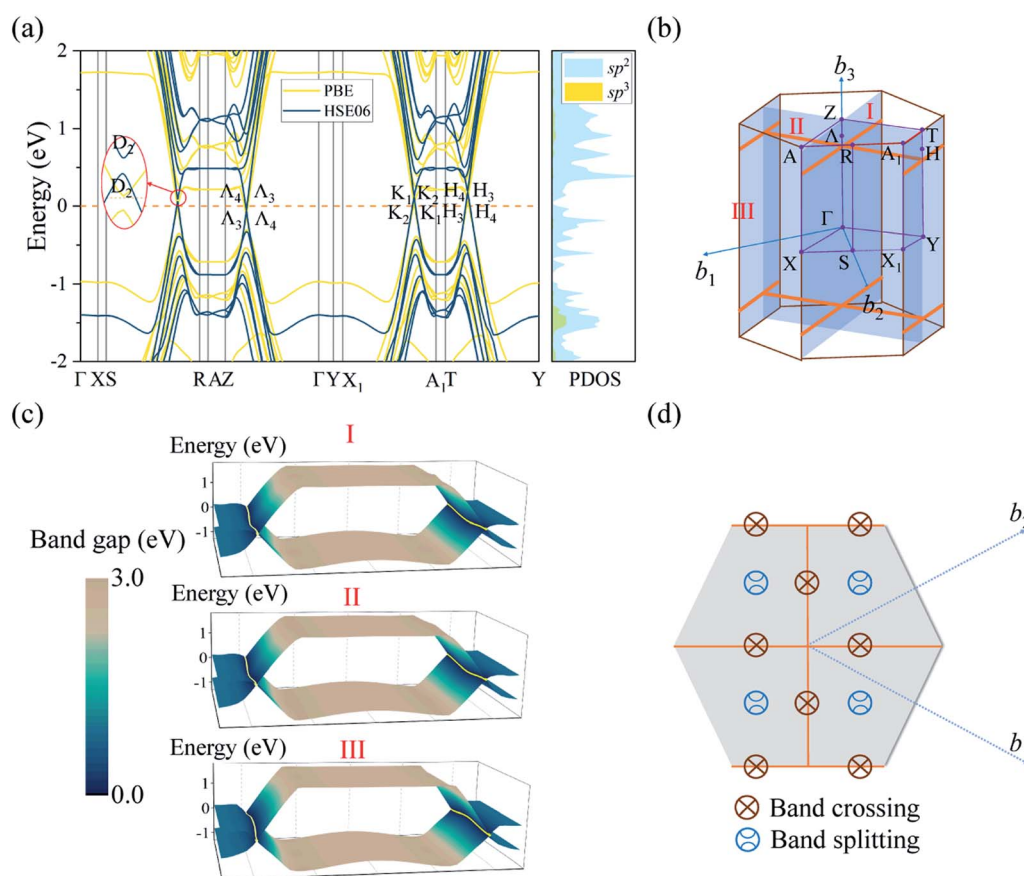


Fig. 4 (a) Electronic band structure, PDOS projected to three-fold coordinated (sp^2) and four-fold coordinated (sp^3) carbon atoms at the PBE level (yellow lines) and the HSE06 level (blue lines) for oC46. (b) First Brillouin zone of oC46, the nodal lines are marked in orange. I, II, and III are the three mirror/glide-invariant planes containing three pairs of nodal lines, respectively. (c) 3D band structures of the VB and CB for the three mirror/glide-invariant planes. The color contour represents the band gap, and the gold lines label the traces of nodal lines. (d) Band-crossing/splitting distribution of the (001)-projected first Brillouin zone.

shows that the band crossing points are secure at the HSE06 level as well. In addition, the partial density of states (PDOS), shown in Fig. 4(a), indicates that the semimetallic feature near the Fermi level mainly originates from the three-fold coordinated carbon atoms. It is worth noting that the conduction band (CB) and valence band (VB) along the high-symmetry paths $Z-\Gamma$, X_1-A_1 , and $T-Y$ belong to the different irreducible

representations as labeled in Fig. 4(a), which results from band inversions, while along the $S-R$ path, the same irreducible representations for the CB and VB lead to prohibiting hybridization of them and then avoiding band crossing. The multiple band-crossing points in the high symmetry k -path indicate that the trace of the Dirac points could potentially be a nodal line, nodal net,²¹ or nodal surface.^{22,23}

To identify the nodal manifold of oC46, we thoroughly scan the entire first Brillouin zone and find three pairs of nodal lines lying in three mirror/glide-invariant planes, *i.e.* plane-I: $k_1 - k_2 = 0$, plane-II: $k_1 + k_2 = 0$, and plane-III: $k_1 - k_2 = 1$ (here we use the fractional coordinates of the first Brillouin zone), and the intersected nodal lines form the nodal net, as shown in Fig. 4(b) (orange lines). Moreover, the 3D band structures and band gap contours of oC46 in the mirror/glide-invariant planes (plane-I, II, and III) are plotted in Fig. 4(c). For each plane, the CB and VB cross along the nodal lines, confirming the validity of the nodal-net feature. On the other hand, the band crossing can also be examined by a symmetry-based method as follows. We firstly lay down several evenly spaced points in the (001)-projected first Brillouin zone as the hexagonal area shown in Fig. 4(d). Each point (x, y) corresponds to a path from $(x, y, 0)$ to $(x, y, 0.5)$ in the first Brillouin zone. Then, we calculate the irreducible representation for each path to identify the band crossing/splitting, *i.e.* if the CB and VB belong to the same irreducible representation near the crossing point along that path, then the band is split. If they belong to two different irreducible representations, the symmetry-protected band crossing will emerge. Thus, it is an effective way to confirm the morphology of the nodal manifold. After careful calculations, the first Brillouin zone can be divided into two parts, *i.e.* orange lines and gray blocks, as shown in Fig. 4(d), where the orange

lines represent the band crossing occurring at each point on these lines, while the gray blocks relate to the band splitting. To probe the anisotropy of carrier mobility, we evaluate the effective mass of carriers, which depends on the flatness of the band. From Fig. 4(c), one can see that the bands near the Fermi level are linearly dispersed in one direction and nearly flat in the orthogonal direction, showing the anisotropy of the effective mass, indicating that the carrier mobility of oC46 is anisotropic, while along the [001] direction, only massless Dirac fermions could be excited by the linear dispersion of the nodal lines. Thus, the electric anisotropy would not affect the carrier mobility along the direction of the nanopores.

To understand the origin of the topological band, the Berry phases around two loops in the first Brillouin zone of oC46 are calculated, as the blue and orange circles shown in Fig. 5(a). Since the spatial inversion, time-reversal symmetries, and spin-rotational symmetry ($SU(2)$) are preserved in oC46, the Berry phase along the loop, which interlocks with a nodal line, should be quantized to $\pm\pi$. This phenomenon could be observed by quantum oscillation experiments.⁴⁶ Any perturbation that maintains time-reversal, spatial inversion, and spin-rotational symmetries will not destroy the band crossing feature, making it robust. As for the net point encircled by the blue loop in Fig. 5(a), the Berry phase is 2π since there are two nodal lines surrounded by the loop. The 2π Berry phase is equivalent to

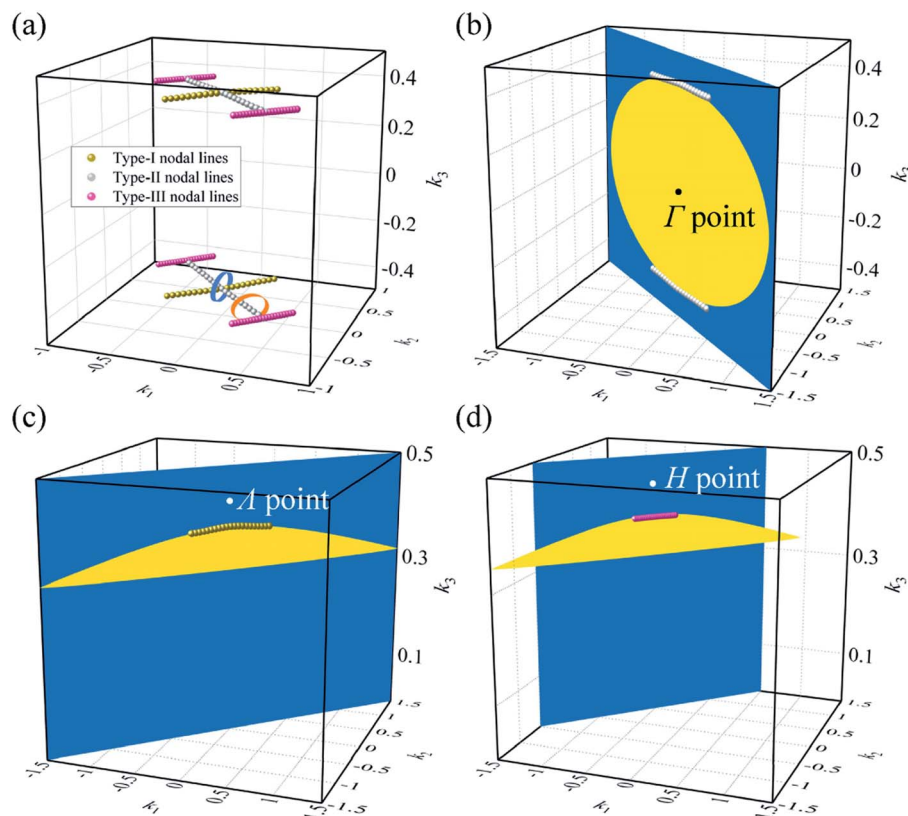


Fig. 5 (a) Calculated nodal lines in the first BZ. The blue and orange loops are two paths along which the Berry phases are calculated. The intersections of the blue plane and yellow surfaces in (b), (c), and (d) are three types of nodal lines derived from three two-band effective $k \cdot p$ Hamiltonians around the Γ (0, 0, 0), A (0, 0, 0.45), and H (-0.5, 0.5, 0.45) points, respectively. The yellow, gray, and pink spheres represent the k -points on the nodal lines calculated by DFT.

0 due to the Z_2 feature of the Berry phase in this nodal-net system. In addition, for each k -point on the nodal net, the irreducible representations of VB and CB are distinguished by distinct mirror/glide-plane symmetry eigenvalues, namely, the nodal net is protected by mirror/glide-plane symmetries.²⁴ The protections of nodal lines by both non-trivial Berry phase and mirror/glide-plane symmetry are so-called two mechanisms.⁴⁷

To get a systematic understanding of the nodal net's origin, we construct the following two-band effective $\mathbf{k}\cdot\mathbf{p}$ model around the Γ point:

$$H^\Gamma(\mathbf{k}) = \sum_{i=0}^3 d_i(\mathbf{k})\sigma_i \quad (1)$$

Here σ_i ($i = x, y, z$) are the Pauli matrices. The little co-group at the Γ point is D_{2h} , including three generators, *i.e.* mirror-plane symmetry M_I , glide-plane symmetry $\{M_{II}|c/2\}$, and inversion P . In addition, the time-reversal symmetry T is also preserved at the Γ point. For a nonmagnetic material without considering SOC, spin could be treated as a dumb index, and thus the time-reversal operator is the complex conjugation operator, *i.e.* $T = K$. The inversion symmetry operator is chosen as $P = \sigma_z$ due to the opposite parities of the two inverted bands at the Γ point. Thus, the coexistence of spatial inversion and time-reversal symmetries (PT -symmetry) requires that:

$$d_1(\mathbf{k}) = 0 \quad (2)$$

$$d_2(\mathbf{k}) = -d_2(-\mathbf{k}) \quad (3)$$

$$d_3(\mathbf{k}) = d_3(-\mathbf{k}) \quad (4)$$

Moreover, as shown in Fig. 4(b), two opposite nodal lines lie in the glide plane (plane-II). According to the eigenvalues of the glide-plane symmetry, we choose $M_{II} = \sigma_z$, leading to:

$$d_2(k_1, k_2, k_3) = -d_2(-k_2, -k_1, k_3) \quad (5)$$

$$d_3(k_1, k_2, k_3) = d_3(-k_2, -k_1, k_3) \quad (6)$$

Similarly, we take $M_I = I$, where I is the identity, which results in:

$$d_i(k_1, k_2, k_3) = d_i(k_2, k_1, k_3), (i = 2, 3) \quad (7)$$

Thus, we have $d_2(\mathbf{k}) = a_1(k_1 + k_2)$, $d_3(\mathbf{k}) = c_0 + c_1(k_1^2 + k_2^2) + c_2k_3^2 + c_3k_1k_2$, where the a_i s ($i = 1$), c_j s ($j = 0, 1, 2, 3$) are constants. The band crossing appears when $d_2(\mathbf{k}) = 0$ and $d_3(\mathbf{k}) = 0$. For $d_2(\mathbf{k}) = 0$, it is the plane-II, *i.e.* $k_1 + k_2 = 0$. As for $d_3(\mathbf{k}) = 0$, it forms an ellipsoid in the Brillouin zone, satisfying all symmetries at the Γ point, and then the two surfaces intersect with each other, forming the type-II nodal lines in plane-II, as shown in Fig. 5(b). Here, we take the fractional coordinates for k -points, which is dimensionless, and the parameters are chosen to be $c_0 = -0.002$ eV, $c_1 = 0.394$ eV, $c_2 = 0.013$ eV, and $c_3 = 0.787$ eV. It shows that the nodal lines derived by the two-band $\mathbf{k}\cdot\mathbf{p}$ model are fitted well with the DFT results, confirming the correctness of our model. In addition, it is easy to prove that the broken glide-plane symmetry will remove the nodal

lines out of the plane $k_1 + k_2 = 0$. When the time-reversal symmetry or inversion symmetry is further broken, the $d_1(\mathbf{k})$ term will be non-zero. According to the generalized von Neumann–Wigner theorem,⁴⁸ the nodal lines will disappear, namely, the type-II nodal lines can be expressed by a two-band model near the Γ point and are protected by the coexistence of PT -symmetry and glide-plane symmetry.

Next, we construct a two-band $\mathbf{k}\cdot\mathbf{p}$ model around the A (0, 0, 0.45) point:

$$H^A(\mathbf{k}) = \sum_{i=0}^3 g_i(\mathbf{k})\sigma_i \quad (8)$$

In this case, the three components (k_1, k_2, k_3) of the momentum \mathbf{k} are relative to the A point. At the A point, the inversion symmetry is absent, and the little co-group is C_{2v} . There are only two generators, *i.e.* mirror-plane symmetry M_I , glide-plane symmetry $\{M_{II}|c/2\}$. In this case, the time-reversal symmetry is also $T = K$. Thus, $g_1(\mathbf{k})$ and $g_3(\mathbf{k})$ are even functions, while $g_2(\mathbf{k})$ is an odd function to \mathbf{k} . Moreover, we take $M_I = \sigma_z$, so that

$$g_1(k_1, k_2, k_3) = -g_1(k_2, k_1, k_3) \quad (9)$$

$$g_2(k_1, k_2, k_3) = -g_2(k_2, k_1, k_3) \quad (10)$$

$$g_3(k_1, k_2, k_3) = g_3(k_2, k_1, k_3) \quad (11)$$

Furthermore, we take $M_{II} = I$, leading to:

$$g_i(k_1, k_2, k_3) = g_i(-k_2, -k_1, k_3), (i = 1, 2, 3) \quad (12)$$

Thus, we have $g_1(\mathbf{k}) = a_2(k_1 - k_2)k_3$, $g_2(\mathbf{k}) = a_3(k_1 - k_2)$, and $g_3(\mathbf{k}) = c_4 + c_5(k_1^2 + k_2^2) + c_6k_3^2 + c_7k_1k_2$, where the a_i s ($i = 2, 3$), c_j s ($j = 4, 5, 6, 7$) are constants. The solution of $g_i(\mathbf{k}) = 0$, ($i = 1, 2, 3$) forming two surfaces, *i.e.* the plane-I: $k_1 - k_2 = 0$ and a hyperboloid: $c_4 + c_5(k_1^2 + k_2^2) + c_6k_3^2 + c_7k_1k_2 = 0$. The type-I nodal lines in the plane-I are the intersections of them, which is consistent with the DFT results, as shown in Fig. 5(c). The model parameters are chosen to be $c_4 = -0.0025$ eV, $c_5 = 0.394$ eV, $c_6 = 0.013$ eV, and $c_7 = 0.787$ eV. Based on the above analysis, only the combination of time-reversal symmetry T and mirror-plane symmetry M_I can eliminate the k_3 term in $g_2(\mathbf{k})$, leading to the intersections (nodal lines) occurring in plane-I. Thus, the type-I nodal lines in the mirror plane are protected by the coexistence of T and M_I . As for type-III nodal lines, we can use a two-band $\mathbf{k}\cdot\mathbf{p}$ model around the H (-0.5, 0.5, 0.45) point, where the little co-group is also C_{2v} with two generators, *i.e.* M_I and $\{M_{II}|c/2\}$. Here, according to the eigenvalues of the two generators, we take $M_I = \sigma_z$ and $M_{II} = I$. Thus, the derivation of this model around H is similar to that of A . As shown in Fig. 5(d), the nodal lines are also intersections of the plane-III: $k_1 - k_2 = 1$ and a hyperboloid: $c_8 + c_9(k_1^2 + k_2^2) + c_{10}k_3^2 + c_{11}k_1k_2 = 0$, where $c_8 = -0.002$ eV, $c_9 = -0.297$ eV, $c_{10} = 0.5$ eV, and $c_{11} = 0.59$ eV. Therefore, the type-III nodal lines are protected by the coexistence of time-reversal symmetry T and mirror-plane symmetry M_I . Compared with the recently reported Weyl-like semimetal

IGN with two nodal loops residing in a mirror invariant plane in the first Brillouin zone,⁴⁹ oC46 has three pairs of nodal lines constrained on three intersected mirror/glide planes, which would provide Dirac fermions in the orthogonal directions and improve its electronic transport properties. In addition, as compared to the semimetals with multi-directional Dirac fermions, such as bct-C₄₀ (nodal-net semimetal)⁴³ and tC₂₄ (nodal-surface semimetal),²⁶ oC46 has nodal lines protected only by orthogonal mirror/glide planes, indicating that the breaking of one mirror/glide symmetry will not affect the nodal lines in the orthogonal planes, exhibiting the robustness of the topological quantum state in oC46.

Based on a tight-binding model generated by the Wannier functions,^{37,38} the surface states projected onto the (100) and (010) surfaces of the unit cell, and the corresponding bulk states are calculated by using the iterative Greens function method⁵⁰ with a ten-layer-thick slab. The surface states and the corresponding bulk states are plotted in Fig. 6(a–d), and the projected surface Brillouin zone for the (100) and (010) surfaces is shown in Fig. 6(e). There is more than one surface flat band between the two band-crossing points due to the superposition effect of multiple nodal lines.⁴³ In addition, since no symmetry

protection mechanism is valid on the surface, the flatness of the surface states disappears and the dubbed drumhead surface states are never topologically protected.²⁴ Nevertheless, when used as an anode material, the large density of surface states endows oC46 with high electron conductivity on the surface, which is crucial for improving the rate capability of a battery. In addition, we study the evolution of the nodal net in the presence of SOC, and the results reveal that the band gap of the nodal net induced by SOC is in the order of 1 meV, which is negligibly weak and maintains the nodal-net semimetallicity of oC46.

3.3. Applications as an anode material for SIBs

Considering the robust nodal-net feature and regular porosity of oC46, this structure can be used for the storage and transport of electrons and sodium ions. To this end, we study its applications as an anode material for SIBs. We first study the adsorption of a single Na ion. To avoid interactions between Na ions, we adopt a $1 \times 1 \times 4$ supercell of the oC46's primitive cell. After geometry optimization, we find five stable hollow sites for single-Na adsorption, namely H1–H5, shown in Fig. 7(a and b). The H1, H2, and H5 reside in the large pore, while H3 and H4 are in the small pore. The adsorption energies of them are calculated by using the formula:

$$E_b = (E_{\text{Na}_x\text{-oC46}} - E_{\text{oC46}} - xE_{\text{Na}})/x \quad (13)$$

Here, $E_{\text{Na}_x\text{-oC46}}$, E_{oC46} , and E_{Na} are the energies of x -Na-adsorbed oC46, pristine oC46, and one sodium atom in its bulk phase, respectively. The calculated adsorption energies are -0.74 , -0.40 , -0.81 , -0.86 , and -0.67 eV for the Na ion on H1–H5 sites, respectively. To analyze the charge transfer during Na adsorption, Bader charge analysis⁵¹ for these five sites is performed. The results show that 0.87, 0.89, 0.88, 0.87, and 0.88 electrons are transferred to the substrate for H1–H5, respectively, demonstrating good binding between sodium ions and the oC46 substrate. Furthermore, the strong coulombic repulsion between the Na ions can prevent them from clustering.

Next, the energy barriers for Na-ion diffusion are examined to evaluate the rate capability. We select five symmetry-nonequivalent migration paths along the conducting channels according to the geometry structure of oC46 and its adsorption sites, as shown in Fig. 7(d). The corresponding diffusion energy barriers are calculated by using the CI-NEB method,³⁹ as presented in Fig. 7(e). For all of the five paths, the energy barriers are in the range of 0.05–0.16 eV, comparable to that of tC₂₄ (0.05 eV).²⁶

We then study the maximum Na capacity of oC46 by gradually increasing the Na concentration until the fully Na-intercalated configuration is reached as shown in Fig. 7(c). This configuration is estimated by considering not only the stable adsorption sites, but also the symmetry and distance between the Na ions to avoid clustering among them. In this configuration, 30 Na ions are regularly distributed at H1, H3, and H4 sites in the supercell, leading to the chemical composition of Na₃₀C₁₈₄.

Next, we evaluate the open-circuit voltage (OCV) by using the following formula:

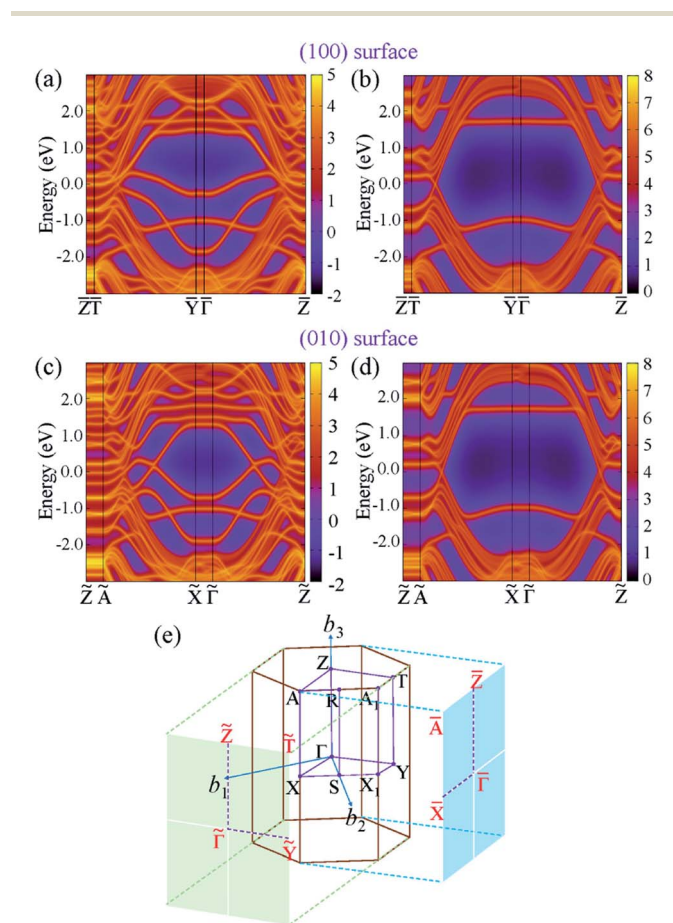


Fig. 6 (a and c) Surface states, and (b and d) corresponding bulk states for the (100) and (010) surfaces, respectively. (e) Bulk Brillouin zone and projected surface Brillouin zone for the (100) and (010) surfaces of the oC46's unit cell, respectively.

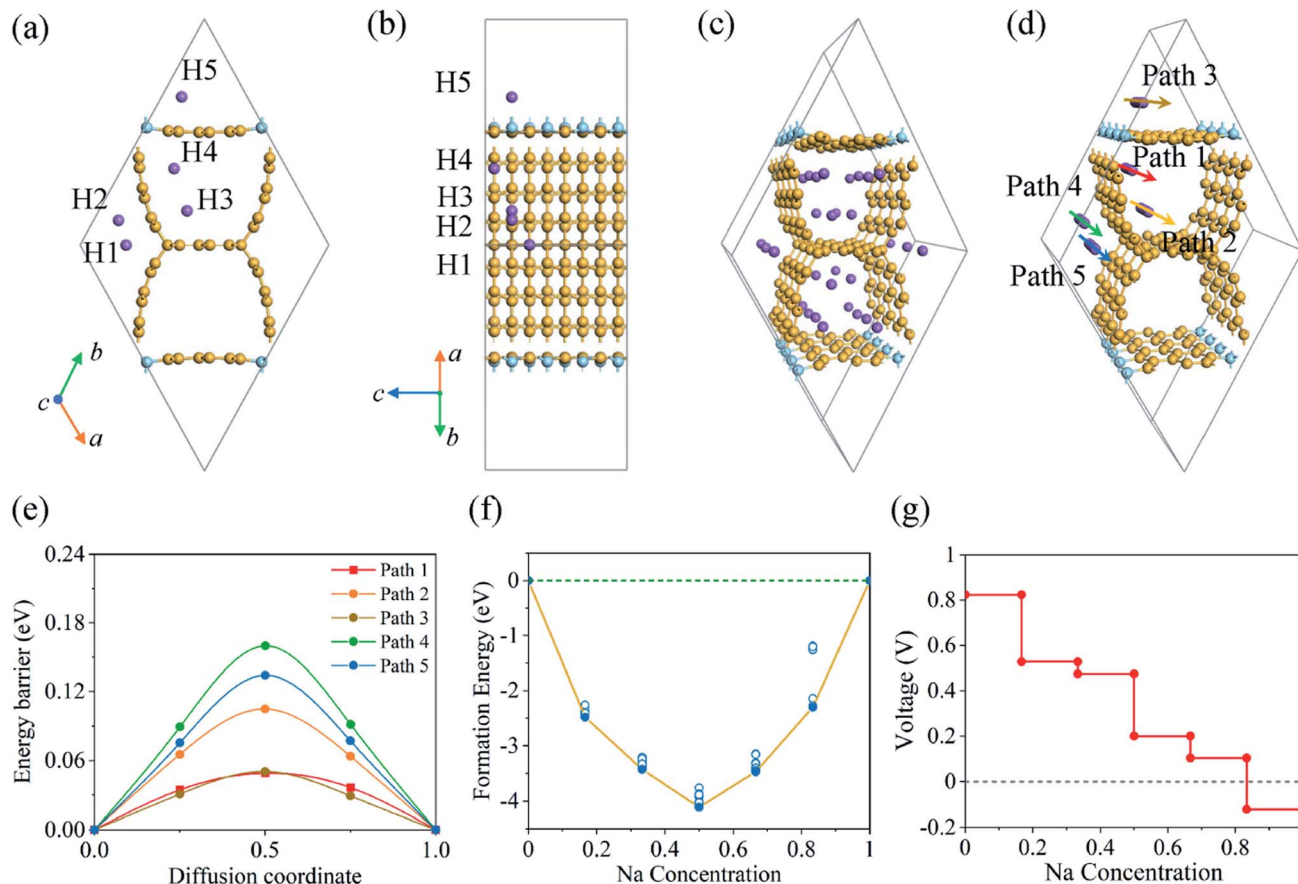


Fig. 7 (a) Top and (b) side views of all possible single Na-ion adsorption sites in oC46. (c) Perspective view of the fully Na-intercalated oC46. (d) Five migration paths for Na-ion diffusion along the conducting channels. (e) Diffusion energy profile for the five paths. (f) Ground-state hull of Na ions in oC46. (g) Calculated voltage profile in the half cell.

$$V \approx - \frac{E_{\text{Na}_{x_2}\text{-oC46}} - E_{\text{Na}_{x_1}\text{-oC46}} - (x_2 - x_1)E_{\text{Na}}}{(x_2 - x_1)e} \quad (14)$$

Here $E_{\text{Na}_{x_2}\text{-oC46}}$, $E_{\text{Na}_{x_1}\text{-oC46}}$, and E_{Na} are the total energies of x_2 -Na-, x_1 -Na-intercalated oC46, and one Na atom in its bulk phase, respectively. To obtain $E_{\text{Na}_{x_2}\text{-oC46}}$ at a certain Na concentration ($\text{Na}_n\text{C}_{6.13}$: $n = 0.167, 0.333, 0.500, 0.667, 0.833$), the optimized structures for these concentrations need to be determined. Thus, we generate 20 symmetry-nonequivalent adsorption configurations at each Na concentration by comparing the electrostatic Ewald energy of them as implemented in the pymatgen package.^{52,53} To probe the charging and discharging processes of oC46, we calculate the formation energy in the ground-state hull by using the formula:⁵⁴ $E_{\text{formation}} = E_c - (1 - c)E_0 - cE_1$, here c is the concentration of Na ions (ranging from 0 to 1), and E_c , E_0 , and E_1 are the energies of Na-intercalated oC46 at the Na concentration of c , 0, and 1, respectively. The ground-state hull diagram of Na ions in oC46 is plotted in Fig. 7(f). The convexity of the hull indicates that the most stable intermediate state obtained by our calculations is the thermodynamic ground state for each Na concentration.⁵⁵ Moreover, the voltage profile of oC46 is presented in Fig. 7(g), which can be divided into two regions: positive region ($0 < n <$

0.833) and negative region ($0.833 < n < 1$). By averaging the voltage in the positive region, the average voltage is 0.43 V, which is lower than that of tC₂₄ (0.54 V)²⁶ and ISN (1.35 V).²⁵ The low OCV is favorable for the anode since it can increase the full cell voltage of the battery. On the other hand, according to the voltage profile, the reversible capacity is 303 mA h g⁻¹, which is still larger than those of tC₂₄ (233 mA h g⁻¹)²⁶ and ISN (160 mA h g⁻¹),²⁵ and large enough for SIB anode applications.

Cycling stability is another key parameter influencing the performance of the battery, which is determined by the volume change of the anode in the Na-adsorption/desorption process. Using the formula $\Delta\Omega = \frac{\Omega_{\text{Na}} - \Omega_0}{\Omega_0} \times 100\%$ (here Ω_{Na} and Ω_0 are the volumes of the fully ($\text{Na}_{30}\text{C}_{184}$) and none (C_{184}) Na-intercalated oC46 configurations, respectively), the calculated volume expansion of oC46 is 2.0%, smaller than that of ISN (2.8%),²⁵ confirming the good cycling stability of oC46.

For clarity, we list four key parameters of oC46 as an anode for SIBs, and compare them with the recently predicted semi-metallic SIB anode materials, *i.e.* ISN (nodal-line semimetal)²⁵ and tC₂₄ (nodal-surface)²⁶ in Table 1. It shows that oC46 possesses a high reversible capacity, low diffusion energy barriers, a low OCV, and a small volume change, indicating that oC46 is a promising candidate for SIB anode materials.

Table 1 Performance comparison of oC46 with two semimetallic anode materials for SIBs

Materials	Reversible capacity (mA h g ⁻¹)	Diffusion barrier (eV)	OCV (V)	Volume change (%)
oC46 nodal-net	303	0.05	0.43	2.0
ISN (ref. 25) nodal-line	160	0.01	1.35	2.8
tC ₂₄ (ref. 26) nodal-surface	233	0.05	0.54	0.9

4. Conclusions

In summary, based on the state-of-the-art theoretical calculations, we report the first study on designing topological nodal-net semimetallic anode materials for SIBs. The structural stability of oC46 is confirmed with phonon spectrum calculation, AIMD simulation, and Born–Huang criteria. oC46 is energetically more favorable over many other 3D semimetallic carbon allotropes. A detailed analysis of its electronic properties reveals that oC46 possesses a nodal net composed of three pairs of nodal lines in its first Brillouin zone, protected by the coexistence of time-reversal, spatial inversion, and mirror/glide-plane symmetries, which can be derived from three effective $\mathbf{k}\cdot\mathbf{p}$ models. Moreover, oC46 exhibits multiple drumhead surface bands, which would enhance the surface electronic conductivity. In addition, we show that oC46 is a promising anode material for SIBs with a high reversible capacity of 303 mA h g⁻¹, much larger than that of graphite (35 mA h g⁻¹), low diffusion energy barriers (0.05–0.16 eV), a relatively low average voltage of 0.43 V, and a negligible volume change (2.0%) as well. This work expands the application of topological quantum materials for Na-ion batteries to nodal-nets with new features.

Conflicts of interest

There are no conflicts of interest to declare.

Acknowledgements

This work is partially supported by a grant from the National Natural Science Foundation of China (Grant No: NSFC-11974028) and the National Key Research and Development Program of the Ministry of Science and Technology of China (2017YFA0205003). It is also supported by the High-Performance Computing Platform of Peking University, China. D. N. thanks Dr Botao Fu from Sichuan Normal University and Dr Xiaoyin Li from the University of Utah for their helpful discussions.

References

- V. Palomares, P. Serras, I. Villaluenga, K. B. Hueso, J. Carretero-González and T. Rojo, Na-ion batteries, recent advances and present challenges to become low cost energy storage systems, *Energy Environ. Sci.*, 2012, **5**, 5884.
- C. Yang, et al., Is graphite nanomesh a promising anode for the Na/K-Ions batteries?, *Carbon*, 2021, **176**, 242.
- Y. Xu, E. Memarzadeh Lotfabad, H. Wang, B. Farbod, Z. Xu, A. Kohandehghan and D. Mitlin, Nanocrystalline anatase

TiO₂: a new anode material for rechargeable sodium ion batteries, *Chem. Commun.*, 2013, **49**, 8973.

- K. Chayambuka, G. Mulder, D. L. Danilov and P. H. L. Notten, Sodium-ion battery materials and electrochemical properties reviewed, *Adv. Energy Mater.*, 2018, **8**, 1800079.
- Q. Sun, Q.-Q. Ren, H. Li and Z.-W. Fu, High capacity Sb₂O₄ thin film electrodes for rechargeable sodium battery, *Electrochem. Commun.*, 2011, **13**, 1462.
- C. Fang, Y. Chen, H.-Y. Kee and L. Fu, Topological nodal line semimetals with and without spin-orbital coupling, *Phys. Rev. B: Condens. Matter Mater. Phys.*, 2015, **92**, 081201.
- K. S. Novoselov, A. K. Geim, S. V. Morozov, D. Jiang, M. I. Katsnelson, I. V. Grigorieva, S. V. Dubonos and A. A. Firsov, Two-dimensional gas of massless Dirac fermions in graphene, *Nature*, 2005, **438**, 197.
- S. M. Young, S. Zaheer, J. C. Y. Teo, C. L. Kane, E. J. Mele and A. M. Rappe, Dirac semimetal in three dimensions, *Phys. Rev. Lett.*, 2012, **108**, 140405.
- X. Wan, A. M. Turner, A. Vishwanath and S. Y. Savrasov, Topological semimetal and Fermi-arc surface states in the electronic structure of pyrochlore iridates, *Phys. Rev. B: Condens. Matter Mater. Phys.*, 2011, **83**, 205101.
- S.-M. Huang, et al., A Weyl Fermion semimetal with surface Fermi arcs in the transition metal monophosphide TaAs class, *Nat. Commun.*, 2015, **6**, 7373.
- S.-Y. Xu, et al., Discovery of a Weyl fermion semimetal and topological Fermi arcs, *Science*, 2015, **349**, 613.
- A. A. Soluyanov, D. Gresch, Z. Wang, Q. Wu, M. Troyer, X. Dai and B. A. Bernevig, Type-II Weyl semimetals, *Nature*, 2015, **527**, 495.
- H. Weng, C. Fang, Z. Fang, B. A. Bernevig and X. Dai, Weyl semimetal phase in noncentrosymmetric transition-metal monophosphides, *Phys. Rev. X*, 2015, **5**, 011029.
- G. Bian, et al., Drumhead surface states and topological nodal-line fermions in TlTaSe₂, *Phys. Rev. B*, 2016, **93**, 121113.
- J. He, X. Kong, W. Wang and S.-P. Kou, Type-II nodal line semimetal, *New J. Phys.*, 2018, **20**, 053019.
- J. Hu, et al., Evidence of topological nodal-line fermions in ZrSiSe and ZrSiTe, *Phys. Rev. Lett.*, 2016, **117**, 016602.
- Z. Yan, R. Bi, H. Shen, L. Lu, S.-C. Zhang and Z. Wang, Nodal-link semimetals, *Phys. Rev. B*, 2017, **96**, 041103.
- R. Bi, Z. Yan, L. Lu and Z. Wang, Nodal-knot semimetals, *Phys. Rev. B*, 2017, **96**, 201305.
- R. Yu, Q. Wu, Z. Fang and H. Weng, From nodal chain semimetal to Weyl semimetal in HfC, *Phys. Rev. Lett.*, 2017, **119**, 036401.
- T. Bzdušek, Q. Wu, A. Rüegg, M. Sigrist and A. A. Soluyanov, Nodal-chain metals, *Nature*, 2016, **538**, 75.

- 21 X. Feng, C. Yue, Z. Song, Q. Wu and B. Wen, Topological Dirac nodal-net fermions in AlB_2 -type TiB_2 and ZrB_2 , *Phys. Rev. Mater.*, 2018, **2**, 014202.
- 22 S.-Z. Chen, S. Li, Y. Chen and W. Duan, Nodal flexible-surface semimetals: case of carbon nanotube networks, *Nano Lett.*, 2020, **20**, 5400.
- 23 C. Zhong, Y. Chen, Y. Xie, S. A. Yang, M. L. Cohen and S. B. Zhang, Towards three-dimensional Weyl-surface semimetals in graphene networks, *Nanoscale*, 2016, **8**, 7232.
- 24 C. Fang, H. Weng, X. Dai and Z. Fang, Topological nodal line semimetals, *Chin. Phys. B*, 2016, **25**, 117106.
- 25 Y. Qie, J. Liu, X. Li, S. Wang, Q. Sun and P. Jena, Interpenetrating silicene networks: A topological nodal-line semimetal with potential as an anode material for sodium ion batteries, *Phys. Rev. Mater.*, 2018, **2**, 084201.
- 26 Y. Qie, J. Liu, S. Wang, Q. Sun and P. Jena, Tetragonal C_{24} : a topological nodal-surface semimetal with potential as an anode material for sodium ion batteries, *J. Mater. Chem. A*, 2019, **7**, 5733.
- 27 G. Kresse and J. Furthmüller, Efficient iterative schemes for *ab initio* total-energy calculations using a plane-wave basis set, *Phys. Rev. B: Condens. Matter Mater. Phys.*, 1996, **54**, 11169.
- 28 P. E. Blöchl, Projector augmented-wave method, *Phys. Rev. B: Condens. Matter Mater. Phys.*, 1994, **50**, 17953.
- 29 J. P. Perdew, K. Burke and M. Ernzerhof, Generalized gradient approximation made simple, *Phys. Rev. Lett.*, 1996, **77**, 3865.
- 30 M. P. Teter, M. C. Payne and D. C. Allan, Solution of Schrödinger's equation for large systems, *Phys. Rev. B: Condens. Matter Mater. Phys.*, 1989, **40**, 12255.
- 31 J. Heyd, G. E. Scuseria and M. Ernzerhof, Hybrid functionals based on a screened Coulomb potential, *J. Chem. Phys.*, 2003, **118**, 8207.
- 32 H. J. Monkhorst and J. D. Pack, Special points for Brillouin-zone integrations, *Phys. Rev. B*, 1976, **13**, 5188.
- 33 K. Parlinski, Z. Q. Li and Y. Kawazoe, First-principles determination of the soft mode in cubic ZrO_2 , *Phys. Rev. Lett.*, 1997, **78**, 4063.
- 34 A. Togo, F. Oba and I. Tanaka, First-principles calculations of the ferroelastic transition between rutile-type and CaCl_2 -type SiO_2 at high pressures, *Phys. Rev. B: Condens. Matter Mater. Phys.*, 2008, **78**, 134106.
- 35 S. H. Zhang and R. F. Zhang, AELAS: Automatic ELASTic property derivations *via* high-throughput first-principles computation, *Comput. Phys. Commun.*, 2017, **220**, 403.
- 36 S. Nosé, A unified formulation of the constant temperature molecular dynamics methods, *J. Chem. Phys.*, 1984, **81**, 511.
- 37 Q. Wu, S. Zhang, H.-F. Song, M. Troyer and A. A. Soluyanov, WannierTools: An open-source software package for novel topological materials, *Comput. Phys. Commun.*, 2018, **224**, 405.
- 38 A. A. Mostofi, J. R. Yates, Y.-S. Lee, I. Souza, D. Vanderbilt and N. Marzari, Wannier90: A tool for obtaining maximally-localised Wannier functions, *Comput. Phys. Commun.*, 2008, **178**, 685.
- 39 G. Mills and H. Jónsson, Quantum and thermal effects in H_2 dissociative adsorption: evaluation of free energy barriers in multidimensional quantum systems, *Phys. Rev. Lett.*, 1994, **72**, 1124.
- 40 J. Liu, X. Li, Q. Wang, Y. Kawazoe and P. Jena, A new 3D Dirac nodal-line semi-metallic graphene monolith for lithium ion battery anode materials, *J. Mater. Chem. A*, 2018, **6**, 13816.
- 41 J.-T. Wang, H. Weng, S. Nie, Z. Fang, Y. Kawazoe and C. Chen, Body-centered orthorhombic C_{16} : A novel topological node-line semimetal, *Phys. Rev. Lett.*, 2016, **116**, 195501.
- 42 J.-T. Wang, C. Chen and Y. Kawazoe, Topological nodal line semimetal in an orthorhombic graphene network structure, *Phys. Rev. B*, 2018, **97**, 245147.
- 43 J.-T. Wang, S. Nie, H. Weng, Y. Kawazoe and C. Chen, Topological nodal-net semimetal in a graphene network structure, *Phys. Rev. Lett.*, 2018, **120**, 026402.
- 44 Z.-Z. Li, J. Chen, S. Nie, L. Xu, H. Mizuseki, H. Weng and J.-T. Wang, Orthorhombic carbon oC_{24} : A novel topological nodal line semimetal, *Carbon*, 2018, **133**, 39.
- 45 Z.-j. Wu, E.-j. Zhao, H.-p. Xiang, X.-f. Hao, X.-j. Liu and J. Meng, Crystal structures and elastic properties of superhard IrN_2 and IrN_3 from first principles, *Phys. Rev. B: Condens. Matter Mater. Phys.*, 2007, **76**, 054115.
- 46 G. P. Mikitik and Y. V. Sharlai, Manifestation of Berry's phase in metal physics, *Phys. Rev. Lett.*, 1999, **82**, 2147.
- 47 X. Zhang, Z.-M. Yu, X.-L. Sheng, H. Y. Yang and S. A. Yang, Coexistence of four-band nodal rings and triply degenerate nodal points in centrosymmetric metal diborides, *Phys. Rev. B*, 2017, **95**, 235116.
- 48 K. Asano and C. Hotta, Designing Dirac points in two-dimensional lattices, *Phys. Rev. B: Condens. Matter Mater. Phys.*, 2011, **83**, 245125.
- 49 Y. Chen, Y. Xie, S. A. Yang, H. Pan, F. Zhang, M. L. Cohen and S. Zhang, Nanostructured carbon allotropes with Weyl-like loops and points, *Nano Lett.*, 2015, **15**, 6974.
- 50 M. P. L. Sancho, J. M. L. Sancho, J. M. L. Sancho and J. Rubio, Highly convergent schemes for the calculation of bulk and surface Green functions, *J. Phys. F: Met. Phys.*, 1985, **15**, 851.
- 51 W. Tang, E. Sanville and G. Henkelman, A grid-based Bader analysis algorithm without lattice bias, *J. Phys.: Condens. Matter*, 2009, **21**, 084204.
- 52 S. P. Ong, et al., Python Materials Genomics (pymatgen): A robust, open-source python library for materials analysis, *Comput. Mater. Sci.*, 2013, **68**, 314.
- 53 S. Wang, Q. Bai, A. M. Nolan, Y. Liu, S. Gong, Q. Sun and Y. Mo, Lithium chlorides and bromides as promising solid-state chemistries for fast ion conductors with good electrochemical stability, *Angew. Chem., Int. Ed.*, 2019, **58**, 8039.
- 54 X. Zhao, X. Zhang, D. Wu, H. Zhang, F. Ding and Z. Zhou, *Ab initio* investigations on bulk and monolayer V_2O_5 as cathode materials for Li-, Na-, K- and Mg-ion batteries, *J. Mater. Chem. A*, 2016, **4**, 16606.
- 55 W. W. Tipton, C. R. Bealing, K. Mathew and R. G. Hennig, Structures, phase stabilities, and electrical potentials of Li-Si battery anode materials, *Phys. Rev. B: Condens. Matter Mater. Phys.*, 2013, **87**, 184114.